

XMM-NEWTON MEASUREMENT OF THE GALACTIC HALO X-RAY EMISSION USING A COMPACT SHADOWING CLOUD

DAVID B. HENLEY, ROBIN L. SHELTON, RENATA S. CUMBEE, AND PHILLIP C. STANCIL
Department of Physics and Astronomy, University of Georgia, Athens, GA 30602; dbh@physast.uga.edu
Draft version March 8, 2021

ABSTRACT

Observations of interstellar clouds that cast shadows in the soft X-ray background can be used to separate the background Galactic halo emission from the local emission due to solar wind charge exchange (SWCX) and/or the Local Bubble (LB). We present an *XMM-Newton* observation of a shadowing cloud, G225.60–66.40, that is sufficiently compact that the on- and off-shadow spectra can be extracted from a single field of view (unlike previous shadowing observations of the halo with CCD-resolution spectrometers, which consisted of separate on- and off-shadow pointings). We analyzed the spectra using a variety of foreground models: one representing LB emission, and two representing SWCX emission. We found that the resulting halo model parameters (temperature $T_h \approx 2 \times 10^6$ K, emission measure $\mathcal{E}_h \approx 4 \times 10^{-3} \text{ cm}^{-6} \text{ pc}$) were not sensitive to the foreground model used. This is likely due to the relative faintness of the foreground emission in this observation. However, the data do favor the existence of a foreground. The halo parameters derived from this observation are in good agreement with those from previous shadowing observations, and from an *XMM-Newton* survey of the Galactic halo emission. This supports the conclusion that the latter results are not subject to systematic errors, and can confidently be used to test models of the halo emission.

Keywords: Galaxy: halo — ISM: clouds — ISM: individual objects (G225.60–66.40) — X-rays: diffuse background — X-rays: ISM

1. INTRODUCTION

An important result from *ROSAT* was the discovery of shadows in the soft X-ray background (SXR), caused by interstellar clouds partially blocking the distant X-ray emission (Burrows & Mendenhall 1991; Snowden et al. 1991). Analysis of such shadows showed that hot, X-ray-emitting plasma exists in the halo of our Galaxy (e.g., Wang & Yu 1995; Kuntz et al. 1997; Snowden et al. 2000). By comparing the X-ray emission observed toward and to the side of a shadowing cloud, one can separate the hot halo emission from the foreground emission, attributable to hot gas in the Local Bubble (LB; Sanders et al. 1977; Snowden et al. 1990), charge exchange (CX) reactions between solar wind ions and neutral H and He in the heliosphere and the Earth’s exosphere (Cravens 2000; Robertson & Cravens 2003a,b; Koutroumpa et al. 2006), or a combination of the two (Smith et al. 2014; Galeazzi et al. 2014). Separating the foreground and halo emission is necessary to test models for the foreground emission, and for the origin of the hot halo plasma.

More recently, *XMM-Newton* and *Suzaku* observations of shadowing clouds have been used to constrain the hot halo emission. These satellites’ CCD cameras have higher spectral resolution than *ROSAT*’s proportional counter. Such studies obtained halo temperatures and emission measures of $\sim 2 \times 10^6$ K and $\sim (3\text{--}12) \times 10^{-3} \text{ cm}^{-6} \text{ pc}$, respectively (Galeazzi et al. 2007; Smith et al. 2007; Gupta et al. 2009; Lei et al. 2009). However, whereas *ROSAT*’s large field of view ($\sim 2^\circ$) meant that a shadowing cloud and the adjacent off-cloud sky could be observed in a single pointing, *XMM-Newton* and *Suzaku*’s smaller fields of view ($\sim 0.5^\circ$ and $\sim 0.3^\circ$, respectively) required that the above-cited shadowing observations consist of two separate pointings—

one toward and one to the side of the cloud under study. While this strategy would be fine if the foreground emission were dominated by a constant source, a time-varying source, solar wind charge exchange (SWCX) emission, is now known to be a major, possibly dominant, contributor to the foreground emission in the *XMM-Newton* and *Suzaku* band (Koutroumpa et al. 2007, 2009, 2011). This SWCX emission is variable on timescales of < 1 day to years (Wargelin et al. 2004; Snowden et al. 2004; Fujimoto et al. 2007; Kuntz & Snowden 2008; Carter & Sembay 2008; Henley & Shelton 2008, 2010, 2012; Carter et al. 2010, 2011; Ezoe et al. 2011). If the foreground SWCX emission varied significantly between the times when the on- and off-shadow pointings were made, the above shadowing analyses would be inaccurate.

In order to ensure that the foreground contribution to the on- and off-shadow emission would be identical, we searched the *COBE*/DIRBE-corrected *IRAS* dust maps (Schlegel et al. 1998) for compact interstellar clouds that would potentially cast an X-ray shadow that would fit within a single *XMM-Newton* field of view. We identified the cloud G225.60–66.40 (G225–66 in Odenwald 1988; G225 hereafter) as a viable target (see Figure 1(a)). The optical depth of this cloud is such that the observed 0.4–1.0 keV surface brightness of the background emission toward the cloud is $\sim 2/3$ of that to the side of the cloud. From simulations we found that such a cloud would be expected to cast a shadow in a ~ 60 ks *XMM-Newton* exposure.¹ Unfortunately, the distance to this cloud is not

¹ Another potentially viable target was [RHK93] 9364 (Reach et al. 1993), at $l = 317^\circ 3$, $b = +83^\circ 8$. However, the contrast between the on- and off-cloud regions within a single *XMM-*

known. Odenwald (1988) assumed a distance of 200 pc; the clouds in his sample for which he was able to estimate distances are at similar distances. If G225 is at a distance of ~ 200 pc, it would be beyond the LB.

Here, we present the *XMM-Newton* observation of this cloud, which we used to constrain the Galactic halo X-ray emission. This is the first measurement of this emission using a single-pointing shadowing observation with a CCD-resolution spectrometer (Anderson et al. (2010) carried out similar observations with *XMM-Newton*, but their target clouds were at low Galactic latitudes ($b \sim 0^\circ.1$), and so measured the disk X-ray emission rather than the halo emission). In particular, we tested the sensitivity of our halo measurement to the assumed foreground model. Recent studies have argued that a combination of LB and SWCX emission is needed to explain the foreground 1/4 keV emission—Smith et al. (2014) and Galeazzi et al. (2014) attributed $\sim 75\%$ and $\sim 40\%$ of the low-Galactic-latitude 1/4 keV foreground to SWCX, respectively. At higher energies, Koutroumpa et al. (2011) attributed approximately half of the foreground O VII emission in an *XMM-Newton* observation of MBM 12 to SWCX. However, the relative contributions of LB and SWCX emission to an arbitrary *XMM-Newton* observation are not known. Therefore, we considered two limiting cases for our foreground model—one in which LB emission dominates, and one in which SWCX emission dominates (for the latter case, we examined two different SWCX models).

The remainder of this paper is organized as follows. The observation and data reduction are described in Section 2. The spectral model and the results from the spectral analysis are presented in Sections 3 and 4, respectively. We discuss our results in Section 5.

2. OBSERVATION AND DATA REDUCTION

G225 was observed by *XMM-Newton* (Jansen et al. 2001) for 90 ks on 2013 Feb 04–06 (observation ID 0690500101). The pointing direction was $(\alpha, \delta) = (02^{\text{h}}39^{\text{m}}20^{\text{s}}.9, -29^{\circ}35'51''.1)$, or $(l, b) = (225^\circ.26, -66^\circ.19)$, toward the north-eastern edge of the cloud (Figure 1(a)).

In our analysis we used data from the EPIC-pn and EPIC-MOS2 cameras (Strüder et al. 2001; Turner et al. 2001; note that during the observation only five out of seven MOS1 CCDs were operating—in particular, the location of one of the inoperative chips meant that $\sim 1/3$ of our on-shadow spectral extraction region [see below] was lost from the MOS1 data). We reduced the data using the *XMM-Newton* Extended Source Analysis Software² (*XMM-ESAS*; Snowden & Kuntz 2013), as included in the Science Analysis System³ (SAS) version 13.5.0. We initially processed the data using the standard SAS `epchain` and `emchain` scripts, and then used the *XMM-ESAS* `pn-filter` and `mos-filter` scripts to remove periods of soft proton flaring, during which the count-rate was elevated. After this filtering, 46.6 and 64.1 ks of good time remained from the pn and MOS2 cameras, respectively.

Newton field was not expected to be as large as for G225. Also, it was not possible to obtain the required exposure from a single pointing.

² http://heasarc.gsfc.nasa.gov/docs/xmm/xmmhp_xmmesas.html

³ <http://xmm.esac.esa.int/sas/>

We used the SAS `edetect_chain` script to detect sources with 0.5–2.0 keV fluxes exceeding 2×10^{-15} erg cm⁻² s⁻¹. Such sources were excluded from the data using circular exclusion regions. For a given source, the source exclusion radius was equal to the semimajor axis of the ellipse on which the source count rate per pixel is 0.2 times the local background count rate. This radius depends on the source brightness relative to the local background. We estimate that the 0.5–2.0 keV surface brightness of the remaining, unremoved background sources is $(3.0 \pm 0.8) \times 10^{-12}$ erg cm⁻² s⁻¹ deg⁻² (90% confidence interval for the whole *XMM-Newton* field). Following Henley & Shelton (2013) and Henley et al. (2014a), we based this estimate on the number density of sources with fluxes of 2.5×10^{-17} to 2×10^{-15} erg cm⁻² s⁻¹ (Moretti et al. 2003) and the measurement of the residual surface brightness after removing sources brighter than 2.5×10^{-17} erg cm⁻² s⁻¹ (Hickox & Markevitch 2006). The uncertainty estimate takes into account the variance in the number of sources due to source clustering (Peebles 1980; Vikhlinin & Forman 1995) in addition to the Poissonian variance—see Henley & Shelton (2013) for details. The above surface brightness is about twice the typical halo surface brightness (Henley & Shelton 2013). The uncertainty on the surface brightness of the unremoved sources does not have a statistically significant effect on our measurements (Section 4).

For each camera, we created an image of the 0.4–1.2 keV quiescent particle background (QPB), using the *XMM-ESAS* `pn_back` and `mos_back` programs. These images were constructed using a database of filter-wheel-closed data, scaled to our observation using data from the unexposed corner pixels that lie outside the field of view (Kuntz & Snowden 2008). We also used the *XMM-ESAS* `proton` program to create images of the residual soft proton contamination that remains despite the filtering described above. The parameters for the soft proton models were determined from the spectral fitting (see Section 3, below). We subtracted the QPB and soft-proton images from the corresponding 0.4–1.2 keV images extracted from our *XMM-Newton* data, divided these background-subtracted images by the corresponding exposure maps, and adaptively smoothed the resulting flat-fielded images (using the *XMM-ESAS* `adapt` program). We filled in the chip gaps and the holes in the data resulting from the source removal using data from neighboring pixels. The resulting X-ray images of G225 from the pn and MOS2 cameras are shown in Figures 1(b) and (c), respectively.

In the pn image one can clearly see the shadow cast by the cloud: there is a deficit of counts where the 100- μm intensity, I_{100} , is greatest. However, the shadow is not apparent in the MOS2 image. This difference between the two cameras' images is not an artifact of the particle background subtraction—the shadow is apparent in the pn image and not the MOS2 image even if we do not subtract the QPB and the soft proton contamination. Instead, the difference is due to the MOS2 camera's lower sensitivity—for a $\sim 2 \times 10^6$ K plasma, say, the 0.4–1.2 keV MOS2 count rate is $\sim 1/5$ the pn rate. We used our best-fit spectral model (with an LB foreground component; see Sections 3.1 and 4, below) to estimate the

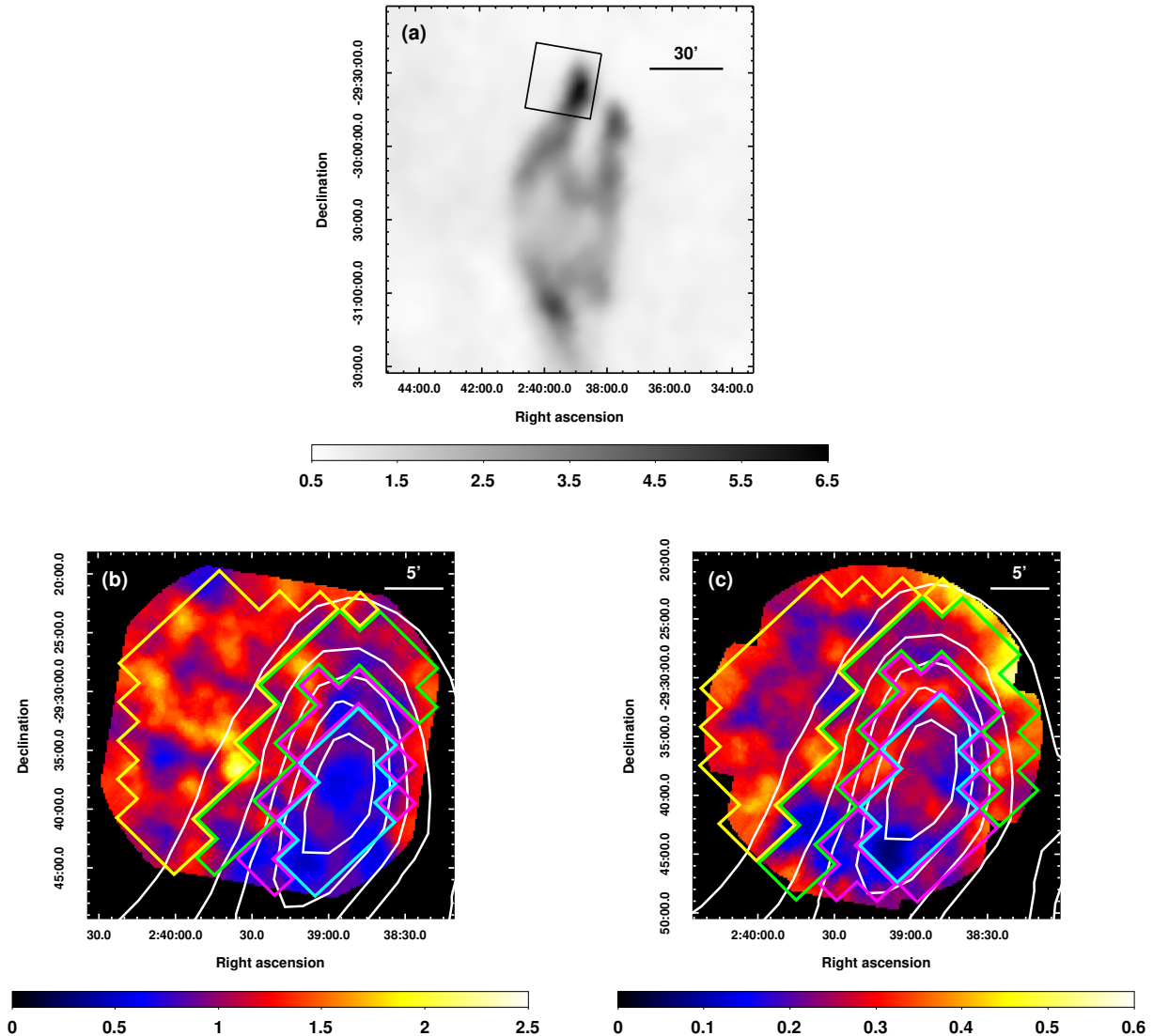


Figure 1. (a) *IRAS* 100- μm image of G225 (Schlegel et al. 1998). The gray scale is in MJy sr^{-1} . The black square indicates the *XMM-Newton* pn field of view. (b) QPB- and soft-proton-subtracted, flat-fielded, adaptively smoothed 0.4–1.2 keV *XMM-Newton* pn image of G225. The chip gaps and the holes in the data resulting from the source removal have been filled using data from neighboring pixels. The color scale is in $\text{counts ks}^{-1} \text{arcmin}^{-2}$. The white contours show the *IRAS* 100- μm intensity ($1\text{--}5 \text{MJy sr}^{-1}$ in one-unit steps). The colored polygons indicate the spectral extraction regions (see text for details). Note that the polygons used for the spectral extraction follow the pixels in the 100- μm map, whereas the contours have been smoothed. (c) As in (b), for MOS2.

count rates expected over the pn and MOS2 fields, taking into account the variation in the absorbing column density of the cloud and the telescope vignetting. While the pn data are indeed expected to exhibit a shadow, the resulting MOS2 count rates are too low to produce a noticeable contrast between the on- and off-shadow regions, given the *XMM-Newton* exposure time.

We extracted X-ray spectra from different regions of the *XMM-Newton* field of view, corresponding to different absorbing column densities, N_{H} . These column densities were derived from the *IRAS* I_{100} map (Schlegel et al. 1998), using the Snowden et al. (2000) I_{100} -to- N_{H} conversion relation. The spectral extraction regions are shown by the colored polygons in Figures 1(b) and (c). These regions outline the I_{100} pixels that correspond to the following N_{H} ranges: < 2 (yellow), 2–4

(green), 4–6 (magenta), and $> 6 \times 10^{20} \text{ cm}^{-2}$ (cyan). Note that, because of the different fields of view, the extraction regions for the MOS2 spectra are slightly different from those for the pn spectra.

From each region we extracted a pn and a MOS2 SXR spectrum, using the *XMM-ESAS pn-spectra* and *mos-spectra* scripts, respectively, and grouped the resulting spectra such that there were at least 50 counts per bin. The spectral extraction scripts also calculated the redistribution matrix file (RMF) and the ancillary response file (ARF) needed for each spectrum, using the *SAS rmfgen* and *arfgen* programs, respectively. For each spectrum, we calculated a corresponding QPB spectrum using the *XMM-ESAS pn_back* and *mos_back* programs. As noted above, the QPB spectra were constructed from a database of filter-wheel-closed

data, scaled using data from the camera pixels outside the field of view. We subtracted from each SXR spectrum the corresponding QPB spectrum before carrying out our spectral analysis.

3. SPECTRAL MODEL DESCRIPTION

In order to separate the foreground and halo emission, we used XSPEC⁴ version 12.8.11 (Arnaud 1996) to fit an SXR spectral model simultaneously to the 0.4–5.0 keV spectra extracted from the different regions of the *XMM-Newton* detectors (we used the spectra from all four regions indicated in Figures 1(b) and (c)). Because the pn image exhibits an X-ray shadow whereas the MOS2 image does not (Figure 1), we investigated fitting to the complete set of pn and MOS2 spectra and fitting just to the pn spectra. We assumed Anders & Grevesse (1989) abundances.

Our SXR spectral model consisted of components representing emission from the foreground, the Galactic halo, and the extragalactic background. We also included components representing parts of the instrumental background that were not removed by the QPB subtraction (see below). As noted in the Introduction, we experimented with different models for the foreground, described in the subsections below. In particular, we considered limiting cases in which LB emission (Section 3.1) or SWCX emission (Sections 3.2 and 3.3) dominate the foreground. The details of the other model components are as follows.

We modeled the Galactic halo emission with a single-temperature (1T) APEC thermal plasma model (Smith et al. 2001; Foster et al. 2012), whose temperature and emission measure were free parameters. We modeled the extragalactic background using the double broken power-law model described in Smith et al. (2007), but with the overall normalization rescaled so that the 0.5–2.0 keV surface brightness matched that expected from sources below the source removal flux threshold of 2×10^{-15} erg cm⁻² s⁻¹ (Henley & Shelton 2013; Henley et al. 2014a); as noted in Section 2, this surface brightness is 3.0×10^{-12} erg cm⁻² s⁻¹ deg⁻². These components were subject to absorption, modeled using the XSPEC `phabs` model (Bałucińska-Church & McCammon 1992; Yan et al. 1998). The absorbing column density, N_{H} , was different for each spectral extraction region, and was calculated from the average value of I_{100} in each region (Schlegel et al. 1998), using the conversion relation from Snowden et al. (2000). These column densities were 1.47 (1.50), 2.78 (2.82), 4.94 (4.96), and $7.00 (7.00) \times 10^{20}$ cm⁻² for the yellow, green, magenta, and cyan regions in Figure 1(b) (Figure 1(c)), respectively. At the energy of the O VII line, the optical depth in the highest- N_{H} region is 0.66, meaning that the halo O VII emission is attenuated by 48%. In the lowest- N_{H} region, the halo O VII emission is attenuated by 13%.

In addition to the above SXR components, we added Gaussians at ~ 1.49 and ~ 1.75 keV to model the Al and Si instrumental fluorescence lines, respectively (note that spectra from the pn detector do not exhibit the Si line). These lines are not included in the QPB spectra calculated using *XMM-ESAS*, and hence were not removed

by the QPB subtraction. The parameters of these lines were independent for each individual spectrum. In order to model any residual soft proton contamination that remained in the spectra despite the filtering described in Section 2, we added a power-law that was not folded through the instrumental response (Kuntz & Snowden 2008; Snowden & Kuntz 2013). For each detector used (pn or MOS2), the spectral index of this component was the same for all four spectra, and the normalizations were tied together according to the relative scaling given by the *XMM-ESAS* `proton_scale` program. The best-fit parameters of this soft proton component were used to create the soft proton images mentioned in Section 2, which were used in the creation of Figures 1(b) and (c).

3.1. Foreground Model 1: Local Bubble (LB)

We initially modeled the foreground emission with a 1T APEC thermal plasma model that was not subject to any absorption. The temperature and emission measure of this component were free parameters. Physically, this model represents emission from a hot plasma, like that thought to be in the LB. Although SWCX is now known to be a major, possibly dominant, source of the foreground emission in the *XMM-Newton* band (Koutroumpa et al. 2007, 2009, 2011), such a thermal plasma model has been found to adequately model the foreground emission in CCD-resolution SXR spectra (e.g., Galeazzi et al. 2007; Henley & Shelton 2008; Gupta et al. 2009). Note that we assumed that the LB emission originates entirely in front of the cloud.

3.2. Foreground Model 2: C14-SWCX

While using a thermal plasma model for the foreground emission appears to provide adequate fits to CCD-resolution SXR spectra, it is possible that the true shape of the foreground spectrum, likely dominated by SWCX emission, is different from that expected from a hot plasma. If this is the case, then a thermal plasma model for the foreground could lead to biases in the best-fit halo parameters. Therefore, in an attempt to avoid such biases, we modified our original SXR model so that the foreground component was composed of CX emission lines. For this model, we use CX line ratio data from Cumbee et al. (2014, hereafter C14; in that paper, we applied our CX data to a *Suzaku* observation of the Cygnus Loop, the spectrum of which is different from that of the SWCX emission). We refer to this new foreground model, which is more physically justified than a thermal plasma model, as the C14-SWCX model.

This foreground SWCX model consisted of C VI Ly α – ϵ , O VII K α – ϵ , and O VIII Ly α – ϵ emission lines. For the O VII K α feature, we modeled the forbidden, intercombination, and resonance lines individually. The overall normalization of the emission from each ion was independent (i.e., we did not constrain the ion ratios *a priori*). For each ion, we tied together the lines' normalizations using the relative intensities from the CX model described in C14.⁵ These CX line ratios were calculated for a collision energy of 1 keV u⁻¹ (438 km s⁻¹; cf. a typical speed for the slow solar wind is 400 km s⁻¹; e.g.,

⁵ Note that the model used here includes C VI Ly ϵ , which was not included in C14. The C VI Ly ϵ /Ly α ratio that we used is 0.0012 (R. S. Cumbee & P. C. Stancil, 2014, private communication).

⁴ <http://heasarc.gsfc.nasa.gov/xanadu/xspec/>

Smith et al. 2003). Note that the C14 CX data are for ions interacting with H. However, as He is an order of magnitude less abundant than H, and CX cross-sections involving He are typically smaller than those involving H (e.g., Koutroumpa et al. 2006, Table 1), neglecting interactions between solar wind ions and He should not adversely affect our results. Note also that, because of the relatively poor spectral resolution of the *XMM-Newton* detectors at low energies, we did not include lines from N VI or N VII in the C14-SWCX model (these ions' $K\alpha$ lines lie between those of C VI and O VII).

Carter et al. (2010) and Ezoe et al. (2011) used a similar CX model (based on data from Bodewits 2007) in their analyses of SWCX enhancements observed during an *XMM-Newton* and a *Suzaku* observation, respectively. However, we are unaware of such a model having previously been applied to a shadowing observation.

3.3. Foreground Model 3: ACX-SWCX

Our third and final foreground model used the AtomDB Charge Exchange code (ACX; Smith et al. 2014), and is referred to here as ACX-SWCX. For each ion receiving an electron via CX, the ACX model uses analytic expressions to calculate the most-probable n shell and the distribution of orbital angular momenta, l , for the captured electron (see Smith et al. 2014 for details). This model then calculates the spectrum produced as the electron radiatively cascades to the ground state (mainly using data from AtomDB 2.0.2; Foster et al. 2012). The relative strengths of the lines from different ions of the same element are determined from the ionization balance of the input ion population, which is controlled by the model's temperature parameter, assuming that the relative ion populations are in collisional ionization equilibrium (CIE). The relative strengths of lines from different elements, meanwhile, are governed by the assumed abundances (Anders & Grevesse 1989).

For our purposes, we set the ACX model's `swcx` and `model` flags to 1 and 8, respectively (Smith & Foster 2014). The former setting means that each ion undergoes a single CX reaction on the line of sight, and is the appropriate setting for studying CX in the context of the diffuse SXR. The latter setting means that, if the most-probable n shell for electron capture is not an integer, the captured electrons are distributed between the two nearest n shells. This setting also means that the "Separable" distribution (Smith et al. 2014, Equation (4)) is used for the l distribution.

4. SPECTRAL ANALYSIS RESULTS

The spectral fit results are shown in Table 1, for the LB (Section 3.1), C14-SWCX (Section 3.2), and ACX-SWCX (Section 3.3) foreground models. In addition, we show results obtained with no foreground component in the spectral model ("None"). The upper half of the table shows the results obtained by fitting simultaneously to the pn and MOS2 spectra, while the lower half shows the results obtained by fitting just to the pn spectra. The best-fit foreground model parameters are in columns 2 and 3 for the LB and ACX-SWCX foreground models, and in columns 4–6 for the C14-SWCX foreground model. For all models, the best-fit halo temperature, T_h , and emission measure, \mathcal{E}_h , are in columns 7

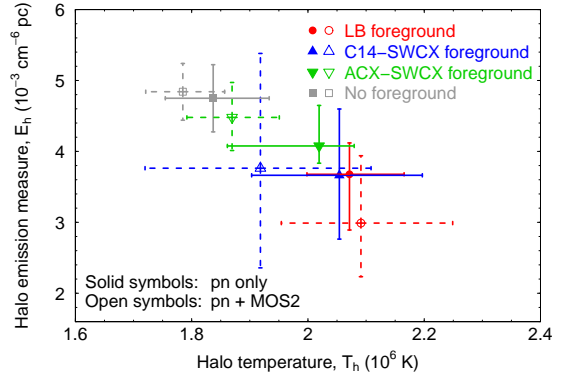


Figure 2. Halo temperatures and emission measures obtained using the various foreground models, indicated by color (see key). Solid symbols and error bars (open symbols and dashed error bars) indicate the results obtained from just the pn data (from the pn and MOS2 data jointly).

and 8, respectively. Figure 2 compares the halo temperatures and emission measures obtained using the various foreground models. Figure 3 shows the pn spectra from the regions with the lowest and highest values of N_H (yellow and cyan regions in Figure 1(b), respectively), along with the best-fit models obtained using each of the three foreground models, and using no foreground model. In general, the fits shown are reasonably good, and the fits to the spectra that aren't shown are of similar quality.

Overall, the pn data result in tighter constraints on the halo parameters when used on their own than when combined with the MOS2 data. The average widths of the 90% confidence intervals on the halo temperature and emission measure are 0.21×10^6 K and 1.2×10^{-3} cm $^{-6}$ pc, respectively, from the pn-only fits, compared with 0.24×10^6 K and 1.6×10^{-3} cm $^{-6}$ pc, respectively, from the joint pn + MOS2 fits. This difference may be due to the fact that the soft proton contamination in the MOS2 spectra is more severe than in the pn spectra (Figure 4). Because the pn spectra result in tighter constraints overall on the halo parameters, in the following we shall concentrate on the results obtained from the pn-only fits.

The results in Table 1 were obtained assuming that the 0.5–2.0 keV surface brightness of the extragalactic background is equal to that expected from sources below the source removal flux threshold, 3.0×10^{-12} erg cm $^{-2}$ s $^{-1}$ deg $^{-2}$ (Section 3). The uncertainty on this expected surface brightness is $\pm 0.8 \times 10^{-12}$ erg cm $^{-2}$ s $^{-1}$ deg $^{-2}$ (Section 2). We found that varying the surface brightness of the extragalactic background model within this uncertainty did not have a statistically significant effect on our best-fit model parameters. This was mainly because, if we adjusted the normalization of the extragalactic model, the normalization of the soft proton contamination model adjusted itself to compensate, leaving the other model components not significantly affected.

For the LB foreground model, while the best-fit foreground temperature, T_{fg} , is rather low, within the uncertainty it is consistent with the range of values found from previous shadowing studies ($T_{fg} \sim (0.8\text{--}1.2) \times 10^6$ K; Snowden et al. 2000; Smith et al. 2007; Galeazzi et al. 2007; Henley et al. 2007; Henley & Shelton 2008;

Table 1
Spectral Fit Results

Foreground model (1)	Foreground					Halo		χ^2/dof (9)
	T_{fg} (10^6 K) (2)	Normalization ^a (3)	$I(\text{C VI})^{\text{b}}$ (L.U.) (4)	$I(\text{O VII})^{\text{c}}$ (L.U.) (5)	$I(\text{O VIII})^{\text{d}}$ (L.U.) (6)	T_{h} (10^6 K) (7)	\mathcal{E}_{h} (10^{-3} cm^{-6} pc) (8)	
Joint fits to pn and MOS2 data:								
LB	1.02 (0.64,1.22)	7.81 (4.16,217.37)	2.09 (1.95,2.25)	2.99 (2.23,3.94)	2154.90/2032
C14-SWCX	1.74 (0.48,3.17)	0.61 (0.23,2.03)	0.01 (0.00,0.55)	1.92 (1.72,2.11)	3.76 (2.36,5.38)	2164.40/2031
ACX-SWCX	0.63 (<0.78)	1.36 (>0.35)	1.87 (1.79,1.95)	4.48 (4.01,4.97)	2160.83/2032
None	1.78 (1.72,1.86)	4.84 (4.44,5.24)	2171.71/2034
Fits to pn data only:								
LB	0.63 (<1.02)	123.35 (>6.97)	2.07 (2.00,2.17)	3.68 (2.89,4.12)	1296.92/1265
C14-SWCX	2.69 (1.93,3.44)	0.57 (0.00,1.67)	0.00 (0.00,0.27)	2.05 (1.90,2.20)	3.66 (2.76,4.60)	1302.90/1264
ACX-SWCX	0.75 (0.53,1.28)	0.29 (0.01,12.23)	2.02 (1.86,2.08)	4.08 (3.83,4.65)	1301.56/1265
None	1.84 (1.75,1.93)	4.75 (4.28,5.22)	1317.11/1267

Note. — Values in parentheses are the 90% confidence intervals.

^a For the LB foreground model, this is the foreground emission measure, \mathcal{E}_{fg} , in units of 10^{-3} cm^{-6} pc. For the ACX-SWCX foreground model, this is the normalization of the foreground component, in units of 10^{-6} arcmin^{-2} .

^b Foreground C VI Ly α intensity. As this line ($E = 0.3673$ keV) is below the *XMM-Newton* band used here, this intensity is not constrained directly, but is instead constrained by the higher-energy Lyman lines via the C14 CX line ratios.

^c Foreground O VII K α intensity. We have summed the intensities of the resonance, intercombination, and forbidden lines.

^d Foreground O VIII Ly α intensity.

Lei et al. 2009; Gupta et al. 2009). Because this foreground model is relatively faint within the *XMM-Newton* band (most of the emission would be emitted below 0.4 keV), its emission measure, \mathcal{E}_{fg} , is poorly constrained. However, it too is consistent (within its uncertainty) with the results from previous shadowing studies.

Although the physical nature of the C14-SWCX foreground model is quite different from that of the LB foreground model, for this particular shadowing observation these two models yield best-fit foreground spectra that are similar in shape in the *XMM-Newton* bandpass (compare Figures 3(a) and (b)). As a result, the best-fit halo parameters from these two models are very similar. However, the halo parameters are less well constrained when we use the C14-SWCX foreground model. This is because, in this model, the foreground C VI, O VII, and O VIII intensities are completely independent, whereas in the LB model they are controlled by the foreground temperature. This means that there is more freedom in the shape of the foreground spectrum, and as a result more freedom in the shape of the halo spectrum, and hence in the halo temperature. Note that the C14-SWCX foreground model yields a higher χ^2 than the LB foreground model, despite having one more free parameter.

The ACX-SWCX foreground model yields a much softer best-fit foreground spectrum than the other foreground models. Since this foreground model produces very little O VII emission, the halo component must produce relatively more O VII, and as a result this foreground model yields a slightly lower halo temperature. However, the difference is only a few $\times 10^4$ K, and is not significant given the error bars.

Figure 5 shows χ^2 as a function of halo temperature for each of the foreground models that we studied. In addition to the best-fit χ^2 minimum at $T_{\text{h}} \approx 2 \times 10^6$ K, each curve also exhibits a local minimum at $T_{\text{h}} \approx 1.2 \times 10^6$ K. At these local minima, the foreground models are harder than in the best fits, to compensate for the softness of the cooler halo models. This means that there is some degeneracy between the hardnesses of the foreground

and halo components. However, the differences in χ^2 between the minima at the lower and higher halo temperatures are 17.8, 7.2, and 19.8 for the LB, C14-SWCX, and ACX-SWCX foreground models, respectively, meaning that the lower halo temperature is excluded at the >99% level ($\Delta\chi^2 = 6.63$ for a single interesting parameter; Lampton et al. 1976). To put this another way, the observed *XMM-Newton* spectra require a soft line-emission component and a hard line-emission component (with temperatures of $\lesssim 1.2 \times 10^6$ and $\sim (2.0\text{--}2.5) \times 10^6$ K, respectively, for models with a temperature parameter). Figure 5 shows that models in which the softer component is in the foreground and the harder component is in the halo (i.e., our best-fitting models, with $T_{\text{h}} \approx 2 \times 10^6$ K) are strongly preferred over models in which these two components are switched.

Because the ACX-SWCX foreground model yields similar halo parameters to the other foreground models, despite the foreground spectrum being much softer, and because omitting the foreground component altogether still yields an acceptable fit (reduced $\chi^2 = 1.04$), one could ask if it is necessary to include a foreground component in the spectral model. To address this question, we used the Akaike Information Criterion (AIC; e.g., Takeuchi 2000; Liddle 2007) to determine the relative quality of the models. The AIC is given by

$$\text{AIC} = -2 \ln \mathcal{L}_{\text{max}} + 2k, \quad (1)$$

where \mathcal{L}_{max} is the maximum likelihood and k is the number of free parameters. The lower the value of AIC, the better the model. As we used χ^2 minimization in our fitting, we make use of the fact that $-2 \ln \mathcal{L}_{\text{max}} = \chi_{\text{min}}^2 + C$, where χ_{min}^2 is the best-fit value of χ^2 , and C is a constant independent of the particular model being considered (as only differences in AIC are meaningful, we can ignore C). For each foreground model, we calculated the AIC relative to that obtained with no foreground model,

$$\Delta\text{AIC}(\text{Model X}) = \text{AIC}(\text{Model X}) - \text{AIC}(\text{No f/g}). \quad (2)$$

For the pn-only fits, the LB, C14-SWCX, and ACX-SWCX foreground models yield $\Delta\text{AIC} = -16.2, -8.2,$

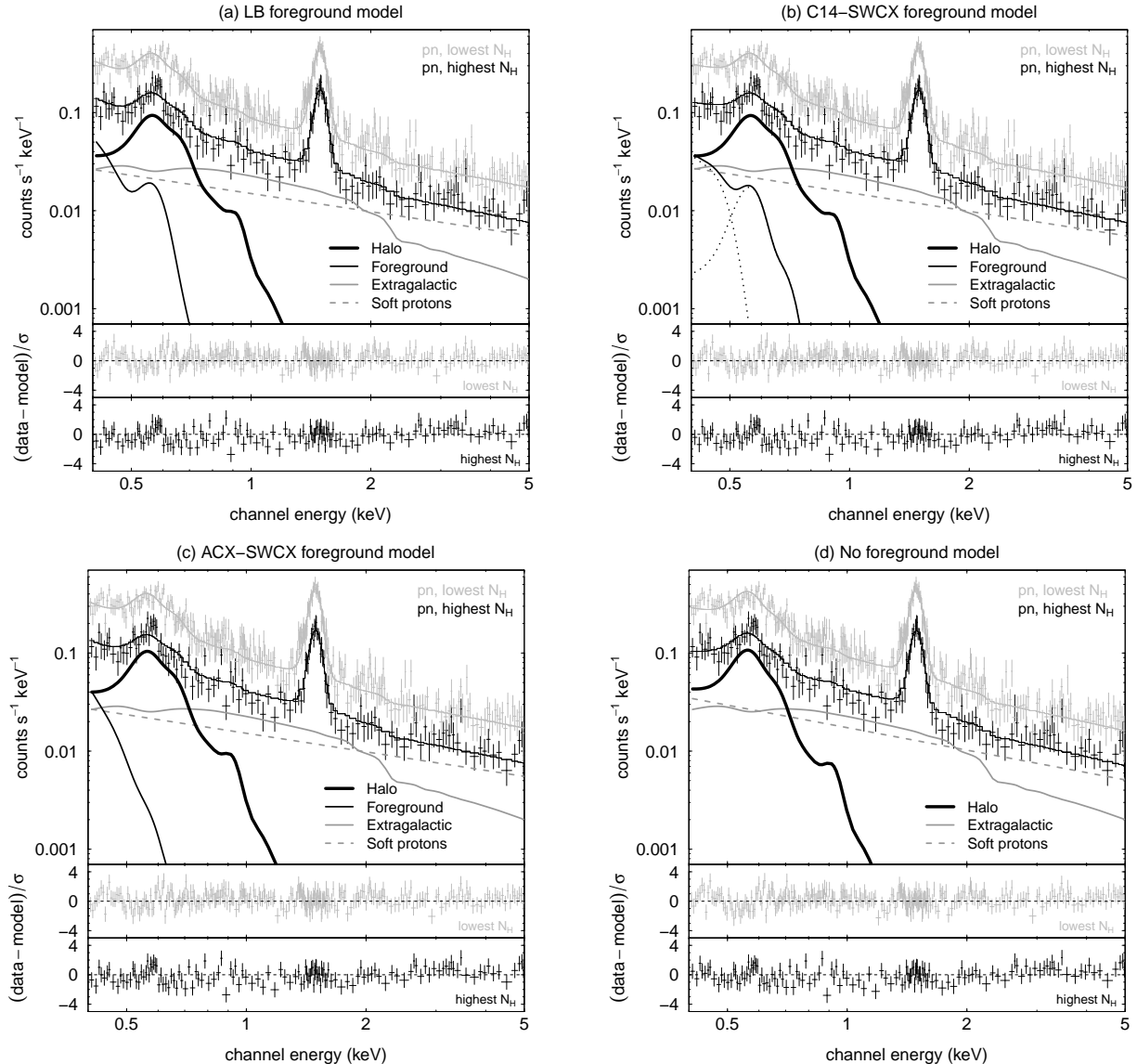


Figure 3. *XMM-Newton* pn spectra from the regions of the G225 field with the lowest and highest values of N_{H} (gray and black data points in the above plots, corresponding to the yellow and cyan regions in Figure 1(b), respectively), with the best-fit spectral models from the fits just to the pn data. For plotting purposes only, the data have been regrouped such that each bin has a signal-to-noise ratio of at least 3. Plots (a), (b), and (c) show the best-fit models obtained with the LB (Section 3.1), C14-SWCX (Section 3.2), and ACX-SWCX (Section 3.3) foreground models, respectively. Plot (d) shows the fit with no foreground component in the spectral model. For the spectrum from the highest- N_{H} region, we also plot individual model components (see key; note that we do not plot the component representing the instrumental Al line). For the SWCX foreground model, the dotted lines show the contributions to the foreground from C VI and O VII (from left to right; the best-fit foreground O VIII intensity is zero).

and -11.6 , respectively. These differences in AIC amount to strong ($\Delta\text{AIC} < -5$) or decisive ($\Delta\text{AIC} < -10$) evidence in favor of including a foreground component in the model (Liddle 2007).

5. DISCUSSION AND CONCLUSIONS

5.1. Foreground Emission

The foreground emission toward G225 appears to be relatively faint in the *XMM-Newton* band. Our spectral analysis implies foreground 0.4–1.0 keV surface brightnesses of 5.0 (2.3–8.8), 4.1 (2.4–8.2), and 2.6 (0.6–4.4) $\times 10^{-13}$ erg cm $^{-2}$ s $^{-1}$ deg $^{-2}$ for the LB, C14-SWCX, and ACX-SWCX foreground models respectively (the values in parentheses are the 90% confidence intervals). In contrast, the results of previous *XMM-Newton* and

Suzaku shadowing studies imply foreground 0.4–1.0 keV surface brightnesses of $(7\text{--}18) \times 10^{-13}$ erg cm $^{-2}$ s $^{-1}$ deg $^{-2}$ (Lei et al. 2009; Gupta et al. 2009; Smith et al. 2007; Galeazzi et al. 2007; Henley et al. 2007). The highest of these is from a pair of *XMM-Newton* pointings on and off an unnamed dusty filament (Henley et al. 2007), which are now known to be contaminated by stronger-than-typical SWCX emission (Koutroumpa et al. 2007; Henley & Shelton 2008).

The faintness of the foreground emission limits the amount of physical information about the foreground that we can extract from our observation of G225. For example, from the C14-SWCX model we obtain only upper limits on the foreground O VII K α and O VIII Ly α intensities, and so we cannot constrain the solar wind

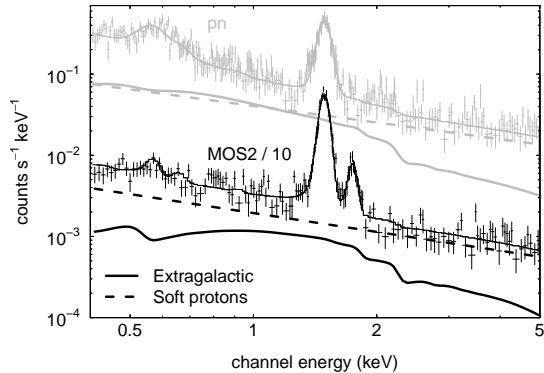


Figure 4. *XMM-Newton* pn (gray) and MOS2 (black) spectra from the region of the G225 field with the lowest value of N_{H} , with the best-fit spectral model obtained with the LB foreground model (thin solid lines). The MOS2 data have been shifted down by a factor of 10. For each spectrum, we also plot the extragalactic and soft proton components of the model (thick solid and dashed lines, respectively; the other model components are not plotted). Note that, in the MOS2 spectrum, the soft proton component is brighter relative to the extragalactic component than in the pn spectrum, indicating more severe soft proton contamination.

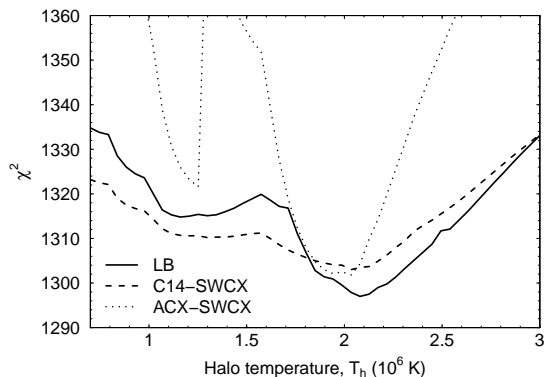


Figure 5. χ^2 as a function of halo temperature for each of the three foreground models that we studied (solid line: LB model; dashed line: C14-SWCX model; dotted line: ACX-SWCX model).

$\text{O}^{8+}/\text{O}^{7+}$ ion ratio using this model. The temperature of the ACX-SWCX model can provide information on this ion ratio, albeit under the assumption of a CIE ion distribution. At the best-fit temperature of the ACX-SWCX component, 7.5×10^5 K, 99% of the oxygen is in the O^{6+} charge state (from ATOMDB v2.0.2; Foster et al. 2012). Assuming CIE therefore results in a best-fit model from which there is virtually no oxygen SWCX emission in the *XMM-Newton* band (the SWCX emission from this model in the *XMM-Newton* band is mainly from N VI $K\alpha$ and C VI Ly β and Ly γ).

We use the upper limit of the temperature of the ACX-SWCX component, 1.28×10^6 K, to place an upper limit of 0.006 on the solar wind $\text{O}^{8+}/\text{O}^{7+}$ ratio (ATOMDB). This is significantly less than the ratio expected for the slow solar wind (0.35; Schwadron & Cravens 2000), suggesting that, during the *XMM-Newton* observation, the portion of the G225 sight line in the heliosphere passed mainly through fast solar wind (for which this ratio is nearly zero; Schwadron & Cravens 2000). This is a somewhat surprising result, as the observation was taken only ~ 9 months before the most recent solar maximum

(based on the sunspot number and the solar 1–8 Å X-ray flux; Winter & Balasubramaniam 2014), at which time the solar wind would be expected mostly to be slow (Smith et al. 2003). Note that the upper limit on the ACX component’s temperature (and hence on the solar wind $\text{O}^{8+}/\text{O}^{7+}$ ratio) is determined not just by the oxygen K lines, but also by lower-energy lines from carbon and nitrogen, and so the low solar wind $\text{O}^{8+}/\text{O}^{7+}$ ratio could in principle be an artifact of our assuming the default Anders & Grevesse (1989) abundances for the ACX model. In practice, this appears not to be the case: if we adjust the abundances of carbon, nitrogen, and neon relative to oxygen⁶ so they match those expected for the slow solar wind (von Steiger et al. 2000, specifically, the average of the “Max” and “Min” values from their Table 1) and refit, we find that the halo results are unaffected, and the resulting upper limit on the solar wind $\text{O}^{8+}/\text{O}^{7+}$ ratio is 0.010, still much lower than the value expected for the slow solar wind. However, we note that the results for the ACX model could be affected by the assumption of an ion distribution described by a single temperature.

It should also be noted that the sun was less active during the most recent maximum than during previous maxima (e.g., the sunspot number and the solar 1–8 Å flux at the most recent maximum were approximately half the values at the 1990 maximum; Winter & Balasubramaniam 2014), which may have affected the solar wind structure. Unfortunately, solar wind charge distribution data from the SWICS instrument on board the *Advanced Composition Explorer* (ACE) are unavailable for times after August 2011,⁷ whereas our observation was taken in February 2013. Therefore, we are unable to check if the solar wind had an unusual ion composition prior to and during our observation.

5.2. Halo Emission

The halo parameters derived from the G225 pn spectra are not sensitive to the particular foreground model used in the analysis, although omitting the foreground component altogether does result in a halo temperature that is $\sim 10\%$ lower. This insensitivity to the details of the foreground model is likely due to the relative faintness of the foreground emission, noted above. If the spectral analysis carried out here were repeated on a shadowing observation with bright foreground emission, we would expect to see some sensitivity of the halo parameters to the assumed form of the foreground emission. We plan to test this in a future study. (Note that this will necessarily involve using shadowing observations that consist of separate on- and off-shadow pointings, unlike the single-pointing observation studied here).

G225 is included in the Snowden et al. (2000) catalog of X-ray shadows in the *ROSAT* All-Sky Survey, as shadow S2267M661.⁸ The intrinsic 1/4 keV halo count rate in the direction of G225 is $(947 \pm 178) \times$

⁶ The absolute abundances of these elements relative to hydrogen are not important here, as hydrogen does not emit in the *XMM-Newton* band. The absolute abundances affect only the overall normalization of the ACX model.

⁷ http://www.srl.caltech.edu/ACE/ASC/level2/lv12DATA_SWICS-SWIMS.html

⁸ This name is derived from the coordinates of the center of the

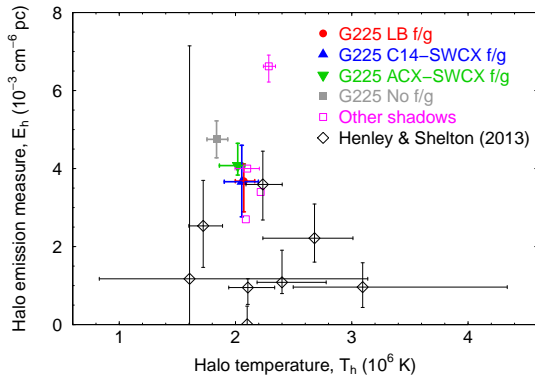


Figure 6. Comparison of our halo measurements with those from previous studies. The solid symbols show our pn-only results from Figure 2. The magenta squares show the results from previous *XMM-Newton* or *Suzaku* shadowing studies: from top to bottom, a *Suzaku* study of an unnamed dusty filament (Lei et al. 2009; note that this result has been rescaled—see text for details), a *Suzaku* study of MBM 12 (Smith et al. 2007), an *XMM-Newton* study of MBM 20 (Galeazzi et al. 2007), and a *Suzaku* study of MBM 20 (Gupta et al. 2009). The black diamonds show results from the Henley & Shelton (2013) *XMM-Newton* survey of the halo, for sight lines within 15° of G225.

10^{-6} counts s^{-1} arcmin $^{-2}$. In contrast, our best fit halo models imply 1/4 keV count rates of $(240\text{--}270) \times 10^{-6}$ counts s^{-1} arcmin $^{-2}$.⁹ This discrepancy implies that a $1T$ model cannot adequately model the halo X-ray emission down to photon energies of ~ 0.1 keV, as was previously demonstrated using *ROSAT* All-Sky Survey data (Kuntz & Snowden 2000). In order to obtain a reasonable model of the 1/4 keV emission, a $\sim 1 \times 10^6$ K component must be added to the halo model—since such a component would contribute to the halo’s O VII emission, its inclusion would affect the best-fit temperature of the $\sim 2 \times 10^6$ K component of our current spectral model. Even such a two-temperature model is likely an approximation of the halo’s true temperature structure, as there may be a continuum of temperatures in the halo (Shelton et al. 2007; Lei et al. 2009). However, the $1T$ halo model used here is still useful for characterizing the emission within the 0.4–5.0 keV *XMM-Newton* band, and the results obtained from such halo models can still be used to test models of the hot halo gas, provided such models’ emission predictions are characterized in the same way as the observed emission (Henley et al. 2010).

Figure 6 compares our measurements with those from previous *XMM-Newton* and *Suzaku* shadowing studies. In these studies, the halo emission was characterized with a single X-ray temperature. The Lei et al. (2009) result was obtained using a different abundance table from the other studies (Wilms et al. 2000 versus Anders & Grevesse 1989¹⁰). The halo emission is dominated in the *XMM-Newton/Suzaku* band by oxygen *K α* emission; for a given temperature, the intensity of this

region of the sky analyzed by Snowden et al. (2000), rather than from the coordinates of the cloud.

⁹ These were calculated using v2.0.2 of APEC (Foster et al. 2012). If we instead use the Raymond & Smith (1977 and updates) code, we obtain count rates $\sim 30 \times 10^{-6}$ counts s^{-1} arcmin $^{-2}$ higher.

¹⁰ Note that Gupta et al. (2009) do not explicitly state which abundance table they used for their plasma emission components.

emission is proportional to $\int n_e n_O dl = \mathcal{E}_h A_O / 1.2$, where n_e and n_O are the halo electron and oxygen number densities, respectively, $\mathcal{E}_h \equiv \int n_e^2 dl$ is the halo emission measure, and A_O is the halo oxygen abundance. Hence, the best-fit halo emission measure is approximately inversely proportional to the assumed value of A_O . Therefore, in order to allow a fair comparison with the other results, we have multiplied the Lei et al. (2009) emission measure by $A_O(\text{Wilms et al.})/A_O(\text{Anders \& Grevesse}) = 0.576$.

In general, our results are in good agreement with those from previous *XMM-Newton* and *Suzaku* shadowing studies. This agreement implies that the fact that these other studies consisted of two separate pointings, which could potentially have had different foreground brightnesses (see Introduction), did not adversely affect the halo results. However, as noted above, the halo results derived from these other studies may be sensitive to the assumed foreground model.

Figure 6 also compares our measurements with results for nearby sight lines in the Henley & Shelton (2013) *XMM-Newton* survey of the halo (within 15° of G225). In this survey, the foreground model was based on results from the previously mentioned Snowden et al. (2000) shadow catalog, extrapolated from the 1/4 keV *ROSAT* band to the 0.4–5.0 keV *XMM-Newton* band. The Henley & Shelton (2013) emission measures shown in Figure 6 are typically smaller than that obtained from G225. One might therefore conclude that there is a systematic error in the Henley & Shelton emission measures, possibly due to the assumed foreground model. However, the Henley & Shelton result that is closest to the G225 results in Figure 6 (obs. 0302500101, at $(T_h, \mathcal{E}_h) = (2.2 \times 10^6 \text{ K}, 3.6 \times 10^{-3} \text{ cm}^{-6} \text{ pc})$) is also the closest sight line to G225 on the sky (angular separation = 4.8°). Hence, it may simply be that the halo within a few degrees of G225 is somewhat brighter than its surroundings. (Note that this does not preclude the possibility that other, more distant regions of the halo are also bright—the other shadows whose results are plotted in Figure 6 are $\sim 30\text{--}50^\circ$ from G225.) Furthermore, the agreement between the G225 measurements and the measurement from the nearest Henley & Shelton (2013) sight line supports the conclusion that the Henley & Shelton results are well calibrated and not subject to systematic errors. Such a conclusion is important for when we use the Henley & Shelton measurements to test models of the halo X-ray emission (Henley et al. 2014b).

We thank the anonymous referee, whose comments have helped improve this paper. This research is based on observations obtained with *XMM-Newton*, an ESA science mission with instruments and contributions directly funded by ESA Member States and NASA. We acknowledge use of the R software package (R Development Core Team 2008). This research was funded by NASA grant NNX13AF69G, awarded through the Astrophysics Data Analysis Program, and partially supported by NASA grant NNX09AC46G.

REFERENCES

Anders, E., & Grevesse, N. 1989, *Geochim. Cosmochim. Acta*, 53, 197

- Anderson, L. D., Snowden, S. L., & Bania, T. M. 2010, *ApJ*, 721, 1319
- Arnaud, K. A. 1996, in *ASP Conf. Ser. 101, Astronomical Data Analysis Software and Systems V*, ed. G. H. Jacoby & J. Barnes (San Francisco: ASP), 17
- Balucińska-Church, M., & McCammon, D. 1992, *ApJ*, 400, 699
- Bodewits, D. 2007, PhD thesis, University of Groningen
- Burrows, D. N., & Mendenhall, J. A. 1991, *Nature*, 351, 629
- Carter, J. A., & Sembay, S. 2008, *A&A*, 489, 837
- Carter, J. A., Sembay, S., & Read, A. M. 2010, *MNRAS*, 402, 867
- Carter, J. A., Sembay, S., & Read, A. M. 2011, *A&A*, 527, A115
- Cravens, T. E. 2000, *ApJL*, 532, L153
- Cumbee, R. S., Henley, D. B., Stancil, P. C., et al. 2014, *ApJL*, 787, L31 (C14)
- Ezoe, Y., Miyoshi, Y., Yoshitake, H., et al. 2011, *PASJ*, 63, S691
- Foster, A. R., Ji, L., Smith, R. K., & Brickhouse, N. S. 2012, *ApJ*, 756, 128
- Fujimoto, R., Mitsuda, K., McCammon, D., et al. 2007, *PASJ*, 59, S133
- Galeazzi, M., Gupta, A., Covey, K., & Ursino, E. 2007, *ApJ*, 658, 1081
- Galeazzi, M., Chiao, M., Collier, M. R., et al. 2014, *Nature*, 512, 171
- Gupta, A., Galeazzi, M., Koutroumpa, D., Smith, R., & Lallement, R. 2009, *ApJ*, 707, 644
- Henley, D. B., & Shelton, R. L. 2008, *ApJ*, 676, 335
- Henley, D. B., & Shelton, R. L. 2010, *ApJS*, 187, 388
- Henley, D. B., & Shelton, R. L. 2012, *ApJS*, 202, 14
- Henley, D. B., & Shelton, R. L. 2013, *ApJ*, 773, 92
- Henley, D. B., Shelton, R. L., & Kuntz, K. D. 2007, *ApJ*, 661, 304
- Henley, D. B., Shelton, R. L., & Kwak, K. 2014a, *ApJ*, 791, 41
- Henley, D. B., Shelton, R. L., Kwak, K., Hill, A. S., & Mac Low, M.-M. 2014b, *ApJ*, submitted
- Henley, D. B., Shelton, R. L., Kwak, K., Joung, M. R., & Mac Low, M.-M. 2010, *ApJ*, 723, 935
- Hickox, R. C., & Markevitch, M. 2006, *ApJ*, 645, 95
- Jansen, F., Lumb, D., Altieri, B., et al. 2001, *A&A*, 365, L1
- Koutroumpa, D., Acero, F., Lallement, R., Ballet, J., & Kharchenko, V. 2007, *A&A*, 475, 901
- Koutroumpa, D., Lallement, R., Kharchenko, V., & Dalgarno, A. 2009, *SSRv*, 143, 217
- Koutroumpa, D., Lallement, R., Kharchenko, V., et al. 2006, *A&A*, 460, 289
- Koutroumpa, D., Smith, R. K., Edgar, R. J., et al. 2011, *ApJ*, 726, 91
- Kuntz, K. D., & Snowden, S. L. 2000, *ApJ*, 543, 195
- Kuntz, K. D., & Snowden, S. L. 2008, *A&A*, 478, 575
- Kuntz, K. D., Snowden, S. L., & Verter, F. 1997, *ApJ*, 484, 245
- Lampton, M., Margon, B., & Bowyer, S. 1976, *ApJ*, 208, 177
- Lei, S., Shelton, R. L., & Henley, D. B. 2009, *ApJ*, 699, 1891
- Liddle, A. R. 2007, *MNRAS*, 377, L74
- Moretti, A., Campana, S., Lazzati, D., & Tagliaferri, G. 2003, *ApJ*, 588, 696
- Odenwald, S. F. 1988, *ApJ*, 325, 320
- Peebles, P. J. E. 1980, *The Large-Scale Structure of the Universe* (Princeton: Princeton University Press)
- R Development Core Team. 2008, *R: A Language and Environment for Statistical Computing*, R Foundation for Statistical Computing, Vienna, Austria
- Raymond, J. C., & Smith, B. W. 1977, *ApJS*, 35, 419
- Reach, W. T., Heiles, C., & Koo, B.-C. 1993, *ApJ*, 412, 127
- Robertson, I. P., & Cravens, T. E. 2003a, *JGR*, 108 (A10), 8031
- Robertson, I. P., & Cravens, T. E. 2003b, *GeoRL*, 30(8), 1439
- Sanders, W. T., Kraushaar, W. L., Nousek, J. A., & Fried, P. M. 1977, *ApJL*, 217, L87
- Schlegel, D. J., Finkbeiner, D. P., & Davis, M. 1998, *ApJ*, 500, 525
- Schwadron, N. A., & Cravens, T. E. 2000, *ApJ*, 544, 558
- Shelton, R. L., Sallmen, S. M., & Jenkins, E. B. 2007, *ApJ*, 659, 365
- Smith, E. J., Marsden, R. G., Balogh, A., et al. 2003, *Science*, 302, 1165
- Smith, R., & Foster, A. 2014, *The AtomDB Charge Exchange Model* (http://www.atomdb.org/CX/acx_manual.pdf)
- Smith, R. K., Brickhouse, N. S., Liedahl, D. A., & Raymond, J. C. 2001, *ApJL*, 556, L91
- Smith, R. K., Foster, A. R., Edgar, R. J., & Brickhouse, N. S. 2014, *ApJ*, 787, 77
- Smith, R. K., Bautz, M. W., Edgar, R. J., et al. 2007, *PASJ*, 59, S141
- Snowden, S. L., Collier, M. R., & Kuntz, K. D. 2004, *ApJ*, 610, 1182
- Snowden, S. L., Cox, D. P., McCammon, D., & Sanders, W. T. 1990, *ApJ*, 354, 211
- Snowden, S. L., Freyberg, M. J., Kuntz, K. D., & Sanders, W. T. 2000, *ApJS*, 128, 171
- Snowden, S. L., & Kuntz, K. D. 2013, *Cookbook for Analysis Procedures for XMM-Newton EPIC MOS Observations of Extended Objects and the Diffuse Background*, version 5.8 (<ftp://legacy.gsfc.nasa.gov/xmm/software/xmm-esas/xmm-esas.pdf>)
- Snowden, S. L., Mebold, U., Hirth, W., Herbstmeier, U., & Schmitt, J. H. M. M. 1991, *Science*, 252, 1529
- Strüder, L., Briel, U., Dennerl, K., et al. 2001, *A&A*, 365, L18
- Takeuchi, T. T. 2000, *Ap&SS*, 271, 213
- Turner, M. J. L., Abbey, A., Arnaud, M., et al. 2001, *A&A*, 365, L27
- Vikhlinin, A., & Forman, W. 1995, *ApJL*, 455, L109
- von Steiger, R., Schwadron, N. A., Fisk, L. A., et al. 2000, *JGR*, 105, 27217
- Wang, Q. D., & Yu, K. C. 1995, *AJ*, 109, 698
- Wargelin, B. J., Markevitch, M., Juda, M., et al. 2004, *ApJ*, 607, 596
- Wilms, J., Allen, A., & McCray, R. 2000, *ApJ*, 542, 914
- Winter, L. M., & Balasubramaniam, K. S. 2014, *ApJL*, in press (arXiv:1409.2763)
- Yan, M., Sadeghpour, H. R., & Dalgarno, A. 1998, *ApJ*, 496, 1044